Letter

Phonon-mediated *s*-wave superconductivity in the kagome metal CsV_3Sb_5 under pressure

Chongze Wang,[1,2] Yu Jia,[1,3] Zhenyu Zhang,[4] and Jun-Hyung Cho[2,*]

[1]*Joint Center for Theoretical Physics, School of Physics and Electronics, Henan University, Kaifeng 475004, People's Republic of China*
[2]*Department of Physics and Research Institute for Natural Science, Hanyang University, 222 Wangsimni-ro, Seongdong-Ku, Seoul 04763, Republic of Korea*
[3]*Key Laboratory for Special Functional Materials of the Ministry of Education, Henan University, Kaifeng 475004, People's Republic of China*
[4]*International Center for Quantum Design of Functional Materials (ICQD), Hefei National Laboratory for Physical Sciences at Microscale, and Synergetic Innovation Center of Quantum Information and Quantum Physics, University of Science and Technology of China, Hefei 230026, China*

(Received 24 February 2023; revised 26 July 2023; accepted 28 July 2023; published 11 August 2023)

The nature of the superconducting pairing state in the pristine phase of the compressed kagome metal CsV_3Sb_5 under pressure is studied by the Migdal-Eliashberg formalism and density-functional theory calculations. We find that the superconducting gap distribution driven by electron-phonon coupling is anisotropic and nodeless. It is revealed that the V $3d$ and Sb $5p$ orbitals forming the four Fermi surface sheets are strongly coupled to the V-V bond-stretching and V-Sb bond-bending phonon modes. The resultant superconducting gaps associated with V $3d_{xy,x^2-y^2,z^2}$ and $3d_{xz,yz}$ orbitals is larger in their average magnitude and more widely spread compared to that associated with the Sb $5p_z$ orbital. Meanwhile, we find that unconventional superconductivity driven by electron correlation effects is unlikely because the saddle points at the M point near the Fermi level do not generate van Hove singularities in the total density of states. Our findings demonstrate that the superconductivity of compressed CsV_3Sb_5 can be explained by the anisotropic multiband pairing mechanism with conventional phonon-mediated *s*-wave symmetry, evidenced by recent experimental observations at ambient pressure and under pressure.

DOI: 10.1103/PhysRevB.108.L060503

The recently discovered kagome metal series AV_3Sb_5 (A = K, Rb, and Cs) has attracted tremendous attention due to its exotic electronic properties such as topologically nontrivial band structures, chiral charge density wave, and superconductivity (SC) [1–5]. For CsV_3Sb_5, a charge density wave (CDW) transition occurs around 94 K at ambient pressure, followed by an emergence of SC as the temperature decreases to ≈3 K [2]. The competition between the CDW order and the SC has been intensively studied by applying pressure [6–12]. The observed pressure-temperature (P-T) phase diagram shows the existence of two superconducting domes under pressure [8–11]. The first superconducting dome exhibits a maximum superconducting transition temperature (T_c) of ≈8 K around 2 GPa [6,7], while the second one exhibits a maximum T_c of ≈6 K around 45 GPa [8–11]. On the other hand, the CDW order is suppressed under pressure and transforms into the pristine phase at a critical pressure of ≈2 GPa [6,7]. The presence of such a quantum critical point (QCP) beneath the top of the first superconducting dome resembles the P-T phase diagrams of many unconventional superconductors such as heavy fermions [13], organics [14], and iron pnictides [15,16], where an antiferromagnetic QCP lies beneath the superconducting dome. Here, spin fluctuations in the vicinity of magnetically ordered phases have been considered to effectively mediate the formation of Cooper pairs [17,18]. Similarly, for the kagome superconductors, many theories have proposed that electron correlation effects at ambient pressure or CDW fluctuations around the QCP could be an essential ingredient of the superconducting pairing mechanism [19–26]. Meanwhile, several first-principles calculations for CsV_3Sb_5 have showed that the variation of electron-phonon coupling (EPC) around the QCP plays an important role in the formation of the superconducting dome [27–29], supporting a conventional phonon-mediated superconducting mechanism. Thus, the question of whether the nature of SC in CsV_3Sb_5 is unconventional (mediated by electronic interactions) or conventional (mediated by phonons) has been controversial.

The pairing symmetry of SC in CsV_3Sb_5 has also been an issue of intense debate. The symmetry structure of Cooper pairs in a superconducting state can be manifested by the momentum dependence of the superconducting gap Δ. For example, cuprate superconductors have a nodal gap with d-wave pairing symmetry [30,31], while conventional phonon-mediated superconductors have a nodeless gap with *s*-wave pairing symmetry [32]. For CsV_3Sb_5, various experiments have reached different conclusions on the superconducting pairing symmetry. Ultralow temperature thermal conductivity measurements have suggested nodal SC [11],

*Corresponding author: chojh@hanyang.ac.kr

whereas magnetic penetration depth experiments using tunnel diode oscillator techniques have reported nodeless SC [33]. Moreover, scanning tunneling microscopy and spectroscopy (STM/STS) measurements have reported different superconducting features of a nodal V-shaped superconducting gap [34,35] and a nodeless *s*-wave superconducting gap [36].

In this Letter, using first-principles density-functional theory (DFT) calculations [37] together with the Migdal-Eliashberg equations [38–40], we explore the anisotropy and pairing symmetry of the superconducting gap in the pristine phase of the multiband kagome superconductor CsV_3Sb_5 under pressure. Our analysis of the band- and **k**-resolved superconducting gap distributions on the four Fermi surface (FS) sheets identifies the existence of an anisotropic, nodeless superconducting gap. By strong coupling to the V-V bond-stretching and V-Sb bond-bending phonon modes, the V $3d_{xy,x^2-y^2,z^2}$ and $3d_{xz,yz}$ orbitals produce larger size and anisotropy in the superconducting gap than the Sb $5p_z$ orbital. Furthermore, we find that the saddle points at the M point near the Fermi level do not generate van Hove singularities (VHSs) in the total density of states (DOS), thereby excluding the possibility of unconventional superconductivity driven by electron correlation effects due to the Fermi-surface nesting of VHSs between three inequivalent M points. The present results provide a theoretical framework for understanding the conventional phonon-mediated *s*-wave pairing symmetry in the SC of the pristine phase, as recently evidenced by several experimental tools such as STM/STS [36], electrical transport and magnetic penetration depth measurements [41,42], and angle-resolved photoemission spectroscopy (ARPES) [43].

We begin by optimizing the atomic structure of CsV_3Sb_5 at a pressure of 3 GPa using the DFT scheme [44]. Figure 1(a) shows the optimized structure corresponding to the $1 \times 1 \times 1$ pristine phase, which crystallizes in the hexagonal space group $P6/mmm$ (No. 191) with the stacking of the V_3Sb kagome layer containing a triangular Sb (termed $Sb^{(1)}$) sublattice centered on each V hexagon, the Sb (termed $Sb^{(2)}$) honeycomb layers above and below the V_3Sb kagome layer, and the Cs triangular layer. The electronic band structure of this pristine phase is displayed in Fig. 1(b), together with its projection onto V $3d$ and Sb $5p$ orbitals (see Figs. 1(b), 1(c), and S1 in the Suppelmental Material [44]). We find that there exist three Dirac points located at the K point [indicated by the dashed circles in Fig. 1(b)], similar to the previous ARPES data [55–57] measured from the high-temperature pristine phase at ambient pressure. Figures 2(a) and 2(b) show the FS composed of four sheets (designated as FS_1, FS_2, FS_3, and FS_4) at $k_z = 0$ and π/c, respectively. Here, FS_1 forms the cylindrical-like sheet surrounding the Γ-A path in the Brillouin zone [see the right panel in Fig 1(a)], while FS_2, FS_3, and FS_4 change their shapes due to the deformation of electronic states along the k_z direction: i.e., FS_2 (FS_3/FS_4) forms the hexagonal-shaped (circularlike) sheet at $k_z = 0$, but FS_2/FS_4 (FS_3) forms the circularlike (deformed hexagonal-shaped) sheet at $k_z = \pi/c$. In Figs. 2(a) and 2(b), we display the projected FS sheets onto the V $3d$ and Sb $5p$ orbitals. We find that the FS sheets feature different orbital characters: i.e., FS_1 arises mostly from the $Sb^{(1)}$ p_z orbital, FS_2 from the V d_{xy,x^2-y^2,z^2} orbitals, and FS_3 and FS_4 from the V $d_{xz,yz}$ orbitals. It is noticeable that the V d_{xy,x^2-y^2,z^2}

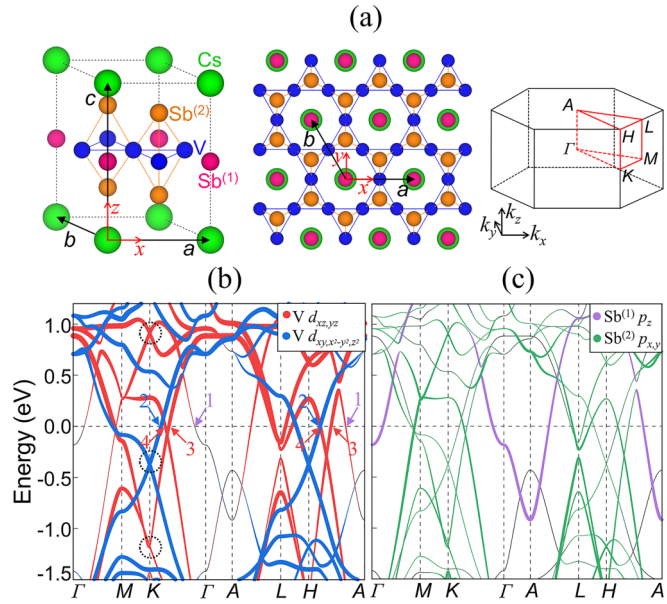

FIG. 1. (a) Optimized structure of the pristine phase of CsV_3Sb_5 at 3 GPa, together with its top view (middle panel) and Brillouin zone (right panel). Here, the lattice parameters are $a = b = 5.410$ Å and $c = 8.563$ Å. (b) Calculated band structure of the pristine phase at 3 GPa. The projected bands onto V $3d$ and Sb $5p$ orbitals are separately displayed in panels (b) and (c), respectively, where the radii of circles are proportional to the weights of the corresponding orbitals. For distinction, the radius scale of Sb $5p$ orbitals is increased by 2 times larger compared to that of V $3d$ orbitals. In panel (b), the numbers indicate band indices forming the FS sheets FS_1, FS_2, FS_3, and FS_4.

and $d_{xz,yz}$ orbitals around E_F hybridize conspicuously with the $Sb^{(2)}$ $p_{x,y}$ orbitals [see Figs. 1(b) and 1(c)] [58]. This hybridization between V $3d$ and Sb $5p$ orbitals leads to an effective electron-phonon interaction between the $V_3Sb^{(1)}$ kagome and $Sb^{(2)}$ honeycomb layers, as discussed below. We also demonstrate later that the presence of such multiple FS sheets with different orbital characters provides a strong anisotropy in EPC, thereby yielding a multiband SC with highly anisotropic superconducting-gap distributions.

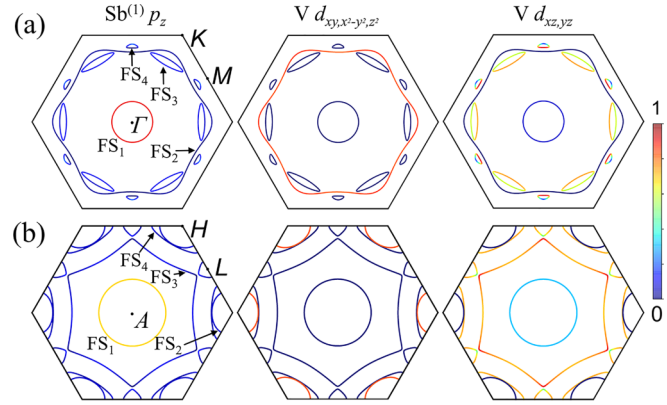

FIG. 2. FS sheets of the pristine phase at 3 GPa, projected onto the $Sb^{(1)}$ $5p_z$, V $3d_{xy,x^2-y^2,z^2}$, and V $3d_{xz,yz}$ orbitals at (a) $k_z = 0$ and (b) π/c using the color scale.

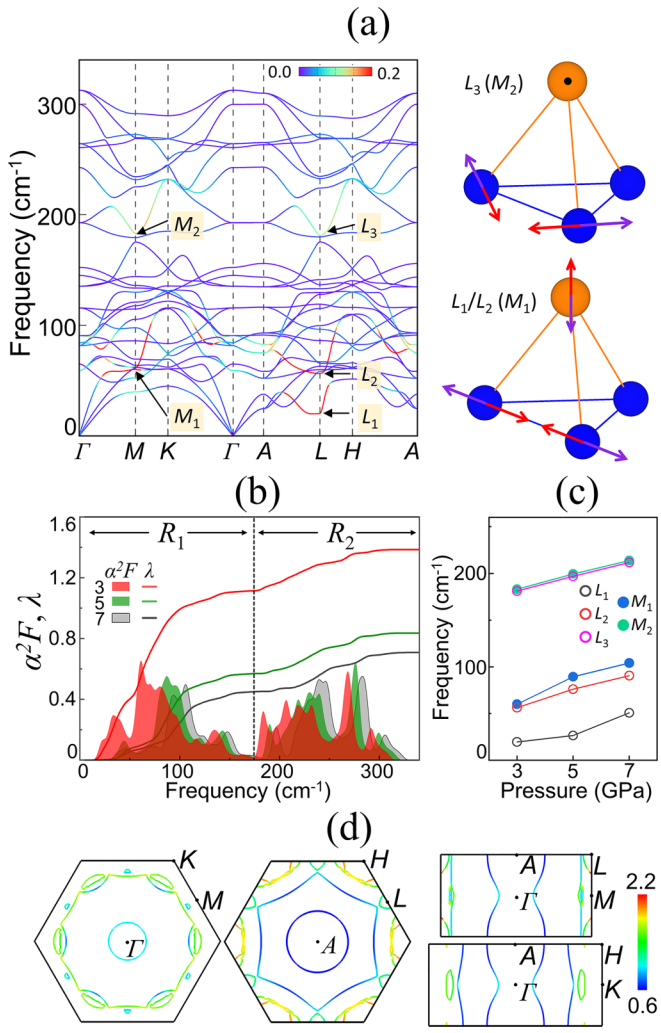

FIG. 3. (a) Calculated phonon spectrum of the pristine phase at 3 GPa, together with the EPC strength (in color scale) of each phonon mode and the main atomic displacements of L_i and M_i ($i = 1$, 2, or 3) modes. Here, L_i and M_i belong to the B_{1u} and A_g modes with D_{2h} symmetry, respectively. The results of α^2F and $\lambda(\omega)$ obtained at 3, 5, and 7 GPa are given in (b). The frequencies of L_i and M_i ($i = 1$, 2, or 3) modes as a function of pressure are displayed in (c). In (d), $\lambda_{n\mathbf{k}}$ on the FS is drawn on the horizontal $k_z = 0$ and $k_z = \pi/c$ planes and the vertical Γ-*M*-*L*-*A* and Γ-*K*-*H*-*A* planes.

To explore the EPC in compressed CsV_3Sb_5, we calculate the phonon spectrum with the EPC strength of each phonon mode, Eliashberg spectral function α^2F, and integrated EPC constant $\lambda(\omega)$ as a function of phonon frequency. The calculated results at 3 GPa are displayed in Figs. 3(a) and 3(b). We find that there are two frequency regimes R_1 and R_2 where $\lambda(\omega)$ increases as large as ≈80% and ≈20% of the total EPC constant $\lambda = \lambda(\infty) = 1.39$, respectively [see Fig. 3(b)]. It is noticeable that the phonon modes L_1, L_2, and M_1 in the low-frequency R_1 regime and L_3 and M_2 in the high-frequency R_2 regime exhibit large EPC strengths. As shown in the right panel of Fig. 3(a), L_1 and M_1 represent the V-V bond-stretching modes coupled with the up and down vibration of $Sb^{(2)}$ atoms; L_2 is similar to L_1 but also involves the relatively larger up and down vibration of Cs atoms approaching $Sb^{(1)}$ atoms; and L_3 and M_2 represent the V-$Sb^{(2)}$ bond-bending modes (see the animation of each mode in the Supplemental Material [44]). As pressure increases, the L_i and M_i ($i = 1$, 2, or 3) phonon modes increase their frequencies [see Fig. 3(c)], yielding a sharp decrease in λ as 0.84 and 0.71 at 5 and 7 GPa, respectively [see Figs. 2(b)]. In other words, as pressure approaches a QCP of ≈2 GPa from higher pressures, the softening of the L_i and M_i phonon modes increases λ, leading to the formation of a superconducting dome around the QCP [6,7,29]. Here, the soft L_i (M_i) modes at the three equivalent L (M) points induce a quantum phase transition to the 2×2×2 CDW phase with the so-called inverse-star-of-David structure [59].

Next, the anisotropy of EPC in compressed CsV_3Sb_5 is examined by using the anisotropic Migdal-Eliashberg equations [38–40]. We calculate the n- and $\mathbf{k}$-resolved EPC constant $\lambda_{n\mathbf{k}}$, which includes all available electron-phonon scattering processes connecting $\mathbf{k}$ and other $\mathbf{k}$ points on the FS_n ($n = 1$, 2, 3, and 4) sheets. Figure 3(d) shows $\lambda_{n\mathbf{k}}$ on the FS_n sheets at 3 GPa. We find that $\lambda_{n\mathbf{k}}$ associated with the $Sb^{(1)}$ p_z orbital ($n = 1$) distributes between ≈0.6 and ≈1.0. Meanwhile, $\lambda_{n\mathbf{k}}$ associated with the V 3*d* orbitals is quite widely spread between ≈0.7 and ≈2.2, where the V ($d_{xz,yz}$: $n = 3$ and 4) and V (d_{xy,x^2-y^2,z^2}: $n = 2$) orbitals are in the ranges of 0.7–1.6 and 1.5–2.2, respectively. Therefore, the EPC strength of the electronic states on the FS sheets varies with respect to their orbital characters and $\mathbf{k}$ directions, indicating a strong anisotropy of the EPC. It is worth noting that this orbital-dependent EPC is attributed to the specific three-dimensional bonding character of the CsV_3Sb_5 kagome crystal: i.e., (i) the V d_{xy,x^2-y^2} (d_{z^2}) orbitals forming the V-V σ (π)-bonding states are effectively coupled to the V-V bond-stretching phonon modes, (ii) the V $d_{xz,yz}$ orbitals hybridizing with the $Sb^{(2)}$ $p_{x,y}$ orbitals [see Figs. 1(b) and 1(c)] are coupled to the V-$Sb^{(2)}$ bond-bending phonon modes, and (iii) the $Sb^{(1)}$ p_z orbital on the FS_1 sheet is coupled to the L_2 phonon mode that involves a decrease in the Cs-$Sb^{(1)}$ distance due to the up and down vibration of Cs atoms, as mentioned above.

It is natural that the wide distribution of $\lambda_{n\mathbf{k}}$ leads to an anisotropy in Δ. By numerically solving the anisotropic Migdal-Eliashberg equations [38–40] with a typical Coulomb pseudopotential parameter of $\mu^* = 0.13$ [29,60,61], we calculate the temperature dependence of Δ at 3 GPa. Figure 4(a) displays the energy distribution of Δ as a function of temperature. We find that the widely distributed Δ closes at a T_c of ≈15 K. To analyze the anisotropy of Δ, we calculate the n- and $\mathbf{k}$-resolved superconducting gap $\Delta_{n\mathbf{k}}$ on the FS sheets at 2 K. As shown in Fig. 4(b), $\Delta_{n\mathbf{k}}$ associated with the $Sb^{(1)}$ p_z ($n = 1$), V $d_{xz,yz}$ ($n = 3$ and 4), and V d_{xy,x^2-y^2,z^2} ($n = 2$) orbitals are in the ranges of 1.5–2.2, 1.6–2.5, and 2.3–3.5 meV, respectively. These band- and $\mathbf{k}$-dependent features of $\Delta_{n\mathbf{k}}$ are well correlated with those of $\lambda_{n\mathbf{k}}$, indicating that the gap size of each band is determined by the strength of the EPC. Therefore, the $\Delta_{n\mathbf{k}}$ distributions on the four FS sheets having different orbital characters are widely spread without any node, representing an anisotropic superconducting gap with *s*-wave pairing symmetry. In Fig. 4(a), the dashed line represents the Δ vs T curve obtained using the isotropic Migdal-Eliashberg formalism [52]. Here, we obtain

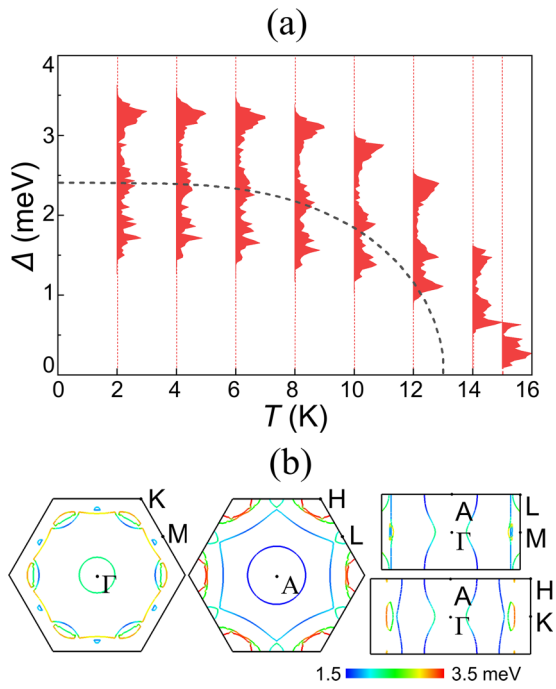

FIG. 4. (a) Calculated energy distribution of the anisotropic superconducting gap as a function of temperature at 3 GPa and (b) $\Delta_{n\mathbf{k}}$ on the FS at 2 K. The dashed line in panel (a) represents Δ values, estimated using the isotropic Migdal-Eliashberg formalism.

$T_c \approx 13$ K, slightly lower than that (≈15 K) estimated using the anisotropic Migdal-Eliashberg formalism. Note that the dimensionless ratio $2\Delta_{T=0}/k_BT_c$ with the isotropic gap and T_c is 4.28 at 3 GPa [62], well comparable with the experimental [41] values of 5.20 and 4.66 at 2.87 and 3.99 GPa, respectively. These theoretical and experimental ratios that are larger than the weak-coupling BCS value of 3.52 indicate a strong-coupling SC in CsV_3Sb_5.

To examine how the characteristics of anisotropic SC vary with increasing pressure, we calculate $\lambda_{n\mathbf{k}}$ and $\Delta_{n\mathbf{k}}$ at 5 GPa. The calculated distribution of $\lambda_{n\mathbf{k}}$ on the FS is displayed in Fig. S3(a) [44]. We find that $\lambda_{n\mathbf{k}}$ values associated with the $Sb^{(1)}$ p_z ($n = 1$), V $d_{xz,yz}$ ($n = 3$ and 4), and V d_{xy,x^2-y^2,z^2} ($n = 2$) orbitals are distributed in the ranges of 0.5–0.9, 0.6–1.0, and 0.8–1.2, respectively. Here, the magnitude and distribution of $\lambda_{n\mathbf{k}}$ arising from V d orbitals are much reduced compared to the corresponding ones at 3 GPa, but the orbital-dependent features of $\lambda_{n\mathbf{k}}$ are similar between 3 and 5 GPa. Due to the reduced $\lambda_{n\mathbf{k}}$ values at 5 GPa, the temperature dependence of Δ closes at $T_c = 9$ K (see Fig. S4) with $2\Delta_{T=0}/k_BT_c \approx 3.83$. Therefore, as pressure increases, $2\Delta_{T=0}/k_BT_c$ is lowered towards the BCS weak-coupling limit. As shown in Fig. S3(b), the $\Delta_{n\mathbf{k}}$ distributions on the FS at 2 K are in the ranges of 1.0–1.7, 1.1–1.6, and 1.4–2.2 meV for the $Sb^{(1)}$ p_z ($n = 1$), V $d_{xz,yz}$ ($n = 3$ and 4), and V d_{xy,x^2-y^2,z^2} ($n = 2$) orbitals, respectively. It is thus likely that the pristine phase at higher pressures preserves the anisotropic superconducting characteristics with s-wave pairing symmetry.

Recently, several experiments [36,42,43] have reported the s-wave superconducting gap symmetry in CsV_3Sb_5 both at ambient pressure and under pressure: i.e., STM/STS [36] reported nodeless s-wave superconductivity with a large anisotropic gap for the V $3d$ orbitals compared to Sb $5p$ orbitals; electrical resistivity and magnetic penetration depth measurements with nonmagnetic impurity effects [42] also provided evidence for the nodeless s-wave superconductivity having an anisotropic (isotropic) gap for V $3d$ (Sb $5p$) orbitals; and ARPES [43] with partial Nb/Ta substitutions of V measured a momentum-dependent superconducting gap to identify a nodeless, nearly isotropic superconducting gap for the V $3d$ and Sb $5p$ orbitals. Despite a difference in the degree of anisotropy in the superconducting gap functions derived from the V $3d$ and Sb $5p$ orbitals, all these experiments [36,42,43] evidenced the nodeless s-wave superconducting symmetry with a non-sign-changing gap. For comparison with such observed superconducting gap distributions, we employ a multigap model with three anisotropic sixfold symmetric gap functions $\Delta_i[1 + \alpha_i\cos(6\phi)]$ [42] originating from the V d_{xy,x^2-y^2,z^2} ($i = 1$), V $d_{xz,yz}$ ($i = 2$), and $Sb^{(1)}$ p_z ($i = 3$) orbitals at 3 GPa. By fitting to the $\Delta_{n\mathbf{k},T=2\mathrm{K}}$ on the FS sheets at $k_z = 0$ [see Fig. 4(b)], we find that the difference between the maximum and minimum gap amplitudes (i.e., $2\alpha_i\Delta_i$) is 0.2, 0.6, and 0.0 meV for $i = 1$, 2, and 3, much smaller than the corresponding Δ_i values of 3.1, 2.0, and 2.3 meV for $i = 1$, 2, and 3, respectively [64]. The resultant anisotropic (isotropic), nodeless superconducting gap for V $3d$ (Sb $5p$) orbitals shows similar characteristics as observed by the abovementioned various experimental techniques [36,42,43].

In summary, our first-principles calculations for the pristine phase of compressed CsV_3Sb_5 have shown that the V $3d_{xy,x^2-y^2,z^2}$, V $3d_{xz,yz}$, and $Sb^{(1)}$ $5p_z$ orbitals forming the multiple FS sheets are strongly coupled to the V-V bond-stretching and V-Sb bond-bending phonon modes, giving rise to the orbital- and momentum-dependent distributions of $\lambda_{n\mathbf{k}}$ and $\Delta_{n\mathbf{k}}$. Therefore, unlike many theories [19–26] favoring unconventional superconductivity in AV_3Sb_5 [66], we pave the way to understanding the superconducting gap symmetry in terms of a conventional phonon-mediated s-wave pairing mechanism. Our findings not only have important implications for understanding the nature of the superconducting pairing state in AV_3Sb_5 [67] but also suggest that EPC would be an important ingredient for the microscopic mechanism of the intertwined CDW and superconducting orders below the QCP. Further theoretical and experimental research efforts are needed to explore the underlying physics of such intertwined orders in AV_3Sb_5.

This work was supported by a grant from the National Research Foundation of Korea (NRF) funded by the Korean Government (Grants No. 2022R1A2C1005456 and No. RS202300218998) and by the BrainLink program funded by the Ministry of Science and ICT through the National Research Foundation of Korea (Grant No. 2022H1D3A3A01077468). Z.Z. acknowledges Innovation Program for Quantum Science and Technology (Grant No. 2021ZD0302800) and Y.J. acknowledges National Natural Science Foundation of China (Grant No. 12074099). The calculations were performed by the KISTI Supercomputing Center through the Strategic Support Program (Program No. KSC-2022-CRE-0073) for the supercomputing application research.

[1] B. R. Ortiz, L. C. Gomes, J. R. Morey, M. Winiarski, M. Bordelon, J. S. Mangum, I. W. H. Oswald, J. A. Rodriguez-Rivera, J. R. Neilson, S. D. Wilson, E. Ertekin, T. M. McQueen, and E. S. Toberer, New kagome prototype materials: Discovery of KV_3Sb_5, RbV_3Sb_5, and CsV_3Sb_5, Phys. Rev. Mater. **3**, 094407 (2019).

[2] B. R. Ortiz, S. M. L. Teicher, Y. Hu, J. L. Zuo, P. M. Sarte, E. C. Schueller, A. M. Milinda Abeykoon, M. J. Krogstad, S. Rosenkranz, R. Osborn, R. Seshadri, L. Balents, J. He, and S. D. Wilson, CsV_3Sb_5: A Z_2 Topological Kagome Metal with a Superconducting Ground State, Phys. Rev. Lett. **125**, 247002 (2020).

[3] Y.-X. Jiang, J.-X. Yin, M. M. Denner, N. Shumiya, B. R. Ortiz, G. Xu, Z. Guguchia, J. He, M. S. Hossain, X. Liu *et al.*, Unconventional chiral charge order in kagome superconductor KV_3Sb_5, Nat. Mater. **20**, 1353 (2021).

[4] B. R. Ortiz, P. M. Sarte, E. M. Kenney, M. J. Graf, S. M. L. Teicher, R. Seshadri, and S. D. Wilson, Superconductivity in the Z_2 kagome metal KV_3Sb_5, Phys. Rev. Mater. **5**, 034801 (2021).

[5] Q. Yin, Z. Tu, C. Gong, Y. Fu, S. Yan, and H. Lei, Superconductivity and normal-state properties of kagome metal RbV_3Sb_5 single crystals, Chin. Phys. Lett. **38**, 037403 (2021).

[6] F. H. Yu, D. H. Ma, W. Z. Zhuo, S. Q. Liu, X. K. Wen, B. Lei, J. J. Ying, and X. H. Chen, Unusual competition of superconductivity and charge-density-wave state in a compressed topological kagome metal, Nat. Commun. **12**, 3645 (2021).

[7] K. Y. Chen, N. N. Wang, Q. W. Yin, Y. H. Gu, K. Jiang, Z. J. Tu, C. S. Gong, Y. Uwatoko, J. P. Sun, H. C. Lei, J. P. Hu, and J.-G. Cheng, Double Superconducting Dome and Triple Enhancement of T_c in the Kagome Superconductor CsV_3Sb_5 under High Pressure, Phys. Rev. Lett. **126**, 247001 (2021).

[8] Z. Zhang, Z. Chen, Y. Zhou, Y. Yuan, S. Wang, J. Wang, H. Yang, C. An, L. Zhang, X. Zhu, Y. Zhou, X. Chen, J. Zhou, and Z. Yang, Pressure-induced reemergence of superconductivity in the topological kagome metal CsV_3Sb_5, Phys. Rev. B **103**, 224513 (2021).

[9] X. Chen, X. Zhan, X. Wang, J. Deng, X. Liu, X. Chen, J. Guo, and X. Chen, Highly robust reentrant superconductivity in CsV_3Sb_5 under pressure, Chinese Phys. Lett. **38**, 057402 (2021).

[10] F. Yu, X. Zhu, X. Wen, Z. Gui, Z. Li, Y. Han, T. Wu, Z. Wang, Z. Xiang, Z. Qiao, J. Ying, and X. Chen, Pressure-Induced Dimensional Crossover in a Kagome Superconductor, Phys. Rev. Lett. **128**, 077001 (2022).

[11] C. C. Zhao, L. S. Wang, W. Xia, Q. W. Yin, J. M. Ni, Y. Y. Huang, C. P. Tu, Z. C. Tao, Z. J. Tu, C. S. Gong, H. C. Lei, Y. F. Guo, X. F. Yang, and S. Y. Li, Nodal superconductivity and superconducting domes in the topological kagome metal CsV_3Sb_5, arXiv:2102.08356.

[12] C. Wang, S. Liu, H. Jeon, and J.-H. Cho, Origin of charge density wave in the layered kagome metal CsV_3Sb_5, Phys. Rev. B **105**, 045135 (2022).

[13] H. Q. Yuan, F. M. Grosche, M. Deppe, C. Geibel, G. Sparn, and F. Steglich, Observation of two distinct superconducting phases in $CeCu_2Si_2$, Science **302**, 2104 (2003).

[14] M. Dressel, Quantum criticality in organic conductors? Fermi liquid versus non-Fermi-liquid behaviour, J. Phys.: Condens. Matter **23**, 293201 (2011).

[15] G. R. Stewart, Superconductivity in iron compounds, Rev. Mod. Phys. **83**, 1589 (2011).

[16] P. Dai, Antiferromagnetic order and spin dynamics in iron-based superconductors, Rev. Mod. Phys. **87**, 855 (2015).

[17] D. D. Osheroff, Superfluidity in ^{3}He: Discovery and understanding, Rev. Mod. Phys. **69**, 667 (1997).

[18] J. R. Schrieffer, X. G. Wen, and S. C. Zhang, Dynamic spin fluctuations and the bag mechanism of high-T_{rmc} superconductivity, Phys. Rev. B **39**, 11663 (1989).

[19] M. L. Kiesel and R. Thomale, Sublattice interference in the kagome Hubbard model, Phys. Rev. B **86**, 121105(R) (2012).

[20] W.-S. Wang, Z.-Z. Li, Y.-Y. Xiang, and Q.-H. Wang, Competing electronic orders on kagome lattices at van Hove filling, Phys. Rev. B **87**, 115135 (2013).

[21] M. L. Kiesel, C. Platt, and R. Thomale, Unconventional Fermi Surface Instabilities in the Kagome Hubbard Model, Phys. Rev. Lett. **110**, 126405 (2013).

[22] T. Neupert, M. M. Denner, J.-X. Yin, R. Thomale, and M. Z. Hasan, Charge order and superconductivity in kagome materials, Nat. Phys. **18**, 137 (2022).

[23] T. Nguyen and M. Li, Electronic properties of correlated kagomé metals AV_3Sb_5 (A = K, Rb, and Cs): A perspective, J. Appl. Phys. **131**, 060901 (2022).

[24] X. Wu, T. Schwemmer, T. Möller, A. Consiglio, G. Sangiovanni, D. D. Sante, Y. Iqbal, W. Hanke, A. P. Schnyder, M. M. Denner, M. H. Fischer, T. Neupert, and R. Thomale, Nature of Unconventional Pairing in the Kagome Superconductors AV_3Sb_5 ($A = K$, Rb, Cs), Phys. Rev. Lett. **127**, 177001 (2021).

[25] R. Tazai, Y. Yamakawa, S. Onari, and H. Kontani, Mechanism of exotic density-wave and beyond-Migdal unconventional superconductivity in kagome metal AV_3Sb_5 (A = K, Rb, Cs), Sci. Adv. **8**, eabl4108 (2022).

[26] L. Zheng, Z. Wu, Y. Yang, L. Nie, M. Shan, K. Sun, D. Song, F. Yu, J. Li, D. Zhao, S. Li, B. Kang, Y. Zhou, K. Liu, Z. Xiang, J. Ying, Z. Wang, T. Wu, and X. Chen, Emergent charge order in pressurized kagome superconductor CsV_3Sb_5, Nature (London) **611**, 682 (2022).

[27] J.-F. Zhang, K. Liu, and Z.-Y. Lu, First-principles study of the double-dome superconductivity in the kagome material CsV_3Sb_5 under pressure, Phys. Rev. B **104**, 195130 (2021).

[28] J.-G. Si, W.-J. Lu, Y.-P. Sun, P.-F. Liu, and B.-T. Wang, Charge density wave and pressure-dependent superconductivity in the kagome metal CsV_3Sb_5: A first-principles study, Phys. Rev. B **105**, 024517 (2022).

[29] C. Wang, S. Liu, H. Jeon, Y. Jia, and J.-H. Cho, Charge density wave and superconductivity in the kagome metal CsV_3Sb_5 around a pressure-induced quantum critical point, Phys. Rev. Mater. **6**, 094801 (2022).

[30] P. A. Lee, N. Nagaosa, and X.-G. Wen, Doping a Mott insulator: Physics of high-temperature superconductivity, Rev. Mod. Phys. **78**, 17 (2006).

[31] B. Keimer, S. A. Kivelson, M. R. Norman, S. Uchida, and J. Zaanen, From quantum matter to high-temperature superconductivity in copper oxides, Nature (London) **518**, 179 (2015).

[32] H. J. Choi, D. Roundy, H. Sun, M. L. Cohen, and S. G. Louie, The origin of the anomalous superconducting properties of MgB_2, Nature (London) **418**, 758 (2002).

[33] W. Y. Duan, Z. Y. Nie, S. S. Luo, F. H. Yu, B. R. Ortiz, L. C. Yin, H. Su, F. Du, A. Wang, Y. Chen, X. Lu, J. J. Ying, S. D. Wilson, X. H. Chen, Y. Song, and H. Q. Yuan, Nodeless superconductivity in the kagome metal CsV_3Sb_5, Sci. China: Phys., Mech. Astron. **64**, 107462 (2021).

[34] H. Chen, H. Yang, B. Hu, Z. Zhao, J. Yuan, Y. Xing, G. Qian, Z. Huang, G. Li, Y. Ye *et al.*, Roton pair density wave in a strong-coupling kagome superconductor, Nature (London) **599**, 222 (2021).

[35] Z. Liang, X. Hou, F. Zhang, W. Ma, P. Wu, Z. Zhang, F. Yu, J.-J. Ying, K. Jiang, L. Shan, Z. Wang, and X.-H. Chen, Three-Dimensional Charge Density Wave and Surface-Dependent Vortex-Core States in a Kagome Superconductor CsV_3Sb_5, Phys. Rev. X **11**, 031026 (2021).

[36] H.-S. Xu, Y.-J. Yan, R. Yin, W. Xia, S. Fang, Z. Chen, Y. Li, W. Yang, Y. Guo, and D.-L. Feng, Multiband Superconductivity with Sign-Preserving Order Parameter in Kagome Superconductor CsV_3Sb_5, Phys. Rev. Lett. **127**, 187004 (2021).

[37] P. Hohenberg and W. Kohn, Inhomogeneous electron gas, Phys. Rev. **136**, B864 (1964); W. Kohn and L. J. Sham, Self-consistent equations including exchange and correlation effects, *ibid.* **140**, A1133 (1965).

[38] A. B. Migdal, Interaction between electrons and lattice vibrations in a normal metal, Sov. Phys. JETP **34**, 996 (1958).

[39] G. M. Eliashberg, Interaction between electrons and lattice vibrations in a superconductor, Sov. Phys. JETP **11**, 696 (1960).

[40] P. B. Allen and B. Mitrović, Theory of superconducting T_c, Solid State Phys. **37**, 1 (1983).

[41] W. Zhang, X. Liu, L. Wang, C. W. Tsang, Z. Wang, S. T. Lam, W. Wang, J. Xie, X. Zhou, Y. Zhao, S. Wang, J. Tallon, K. T. Lai, and S. K. Goh, Nodeless superconductivity in kagome metal CsV_3Sb_5 with and without time reversal symmetry breaking, Nano Lett. **23**, 872 (2023).

[42] M. Roppongi, K. Ishihara, Y. Tanaka, K. Ogawa, K. Okada, S. Liu, K. Mukasa, Y. Mizukami, Y. Uwatoko, R. Grasset, M. Konczykowski, B. R. Ortiz, S. D. Wilson, K. Hashimoto, and T. Shibauchi, Bulk evidence of anisotropic *s*-wave pairing with no sign change in the kagome superconductor CsV_3Sb_5, Nat. Commun. **14**, 667 (2023).

[43] Y. Zhong, J. Liu, X. Wu, Z. Guguchia, J.-.X. Yin, A. Mine, Y. Li, S. Najafzadeh, D. Das, C. Mielke III, R. Khasanov, H. Luetkens, T. Suzuki, K. Liu, X. Han, T. Kondo, J. Hu, S. Shin, Z. Wang, X. Shi *et al.*, Nodeless electron pairing in CsV_3Sb_5-derived kagome superconductors, Nature (London) **617**, 488 (2023).

[44] See Supplemental Material at http://link.aps.org/supplemental/10.1103/PhysRevB.108.L060503 for the calculation method, band projections onto the orbitals of V 3*d* and Sb 5*p* orbitals, $\lambda_{n\mathbf{k}}$ and $\Delta_{n\mathbf{k}}$ on the FS at 5 GPa, Δ vs temperature at 5 GPa, and animation of the L_1, L_2, L_3, M_1, and M_2 phonon modes, which include Refs. [45–54].

[45] G. Kresse and J. Hafner, *Ab initio* molecular dynamics for open-shell transition metals, Phys. Rev. B **48**, 13115 (1993).

[46] G. Kresse and J. Furthmüller, Efficiency of ab-initio total energy calculations for metals and semiconductors using a plane-wave basis set, Comput. Mater. Sci. **6**, 15 (1996).

[47] P. E. Blöchl, Projector augmented-wave method, Phys. Rev. B **50**, 17953 (1994).

[48] J. P. Perdew, K. Burke, and M. Ernzerhof, Generalized Gradient Approximation Made Simple, Phys. Rev. Lett. **77**, 3865 (1996); **78**, 1396(E) (1997).

[49] S. Grimme, J. Antony, S. Ehrlich, and H. Krieg, A consistent and accurate ab initio parametrization of density functional dispersion correction (DFT-D) for the 94 elements H-Pu, J. Chem. Phys. **132**, 154104 (2010).

[50] P. Giannozzi, S. Baroni, N. Bonini, M. Calandra, R. Car, C. Cavazzoni, D. Ceresoli, G. L. Chiarotti, M. Cococcioni, I. Dabo *et al.*, QUANTUM ESPRESSO: A modular and open-source software project for quantum simulations of materials, J. Phys.: Condens. Matter **21**, 395502 (2009).

[51] M. J. van Setten, M. Giantomassi, E. Bousquet, M. J. Verstraete, D. R. Hamann, X. Gonze, and G. M. Rignanese, The PseudoDojo: Training and grading a 85 element optimized norm-conserving pseudopotential table, Comput. Phys. Commun. **226**, 39 (2018).

[52] F. Giustino, M. L. Cohen, and S. G. Louie, Electron-phonon interaction using Wannier functions, Phys. Rev. B **76**, 165108(R) (2007).

[53] E. R. Margine and F. Giustino, Anisotropic Migdal-Eliashberg theory using Wannier functions, Phys. Rev. B **87**, 024505 (2013).

[54] S. Poncé, E. R. Margine, C. Verdi, and F. Giustino, EPW: Electron-phonon coupling, transport and superconducting properties using maximally localized Wannier functions, Comput. Phys. Commun. **209**, 116 (2016).

[55] M. Kang, S. Fang, J.-K. Kim, B. R. Ortiz, S. H. Ryu, J. Kim, J. Yoo, G. Sangiovanni, D. D. Sante, B.-G. Park, C. Jozwiak, A. Bostwick, E. Rotenberg, E. Kaxiras, S. D. Wilson, J.-H. Park, and R. Comin, Twofold van Hove singularity and origin of charge order in topological kagome superconductor CsV_3Sb_5, Nat. Phys. **18**, 301 (2022).

[56] Y. Hu, X. Wu, B. R. Ortiz, S. Ju, X. Han, J. Ma, N. C. Plumb, M. Radovic, R. Thomale, S. D. Wilson, A. P. Schnyder, and M. Shi, Rich nature of Van Hove singularities in Kagome superconductor CsV_3Sb_5, Nat. Commun. **13**, 2220 (2022).

[57] R. Lou, A. Fedorov, Q. Yin, A. Kuibarov, Z. Tu, C. Gong, E. F. Schwier, B. Büchner, H Lei, and S. Borisenko, Charge-Density-Wave-Induced Peak-Dip-Hump Structure and the Multiband Superconductivity in a Kagome Superconductor CsV_3Sb_5, Phys. Rev. Lett. **128**, 036402 (2022).

[58] S. Han, C. S. Tang, L. Li, Y. Liu, H. Liu, J. Gou, J. Wu, D. Zhou, P. Yang, C. Diao, J. Ji, J. Bao, L. Zhang, M. Zhao, M. V. Milošević, Y. Guo, L. Tian, M. B. H. Breese, G. Cao, C. Cai, A. T. S. Wee, and X. Yin, Orbital-hybridization-driven charge density wave transition in CsV_3Sb_5 kagome superconductor, Adv. Mater. **35**, 2209010 (2023).

[59] H. Tan, Y. Liu, Z. Wang, and B. Yan, Charge Density Waves and Electronic Properties of Superconducting Kagome Metals, Phys. Rev. Lett. **127**, 046401 (2021).

[60] P. B. Allen and R. C. Dynes, Transition temperature of strong-coupled superconductors reanalyzed, Phys. Rev. B **12**, 905 (1975).

[61] J. Kortus, I. I. Mazin, K. D. Belashchenko, V. P. Antropov, and L. L. Boyer, Superconductivity of Metallic Boron in MgB_2, Phys. Rev. Lett. **86**, 4656 (2001).

[62] By varying μ^* in the range of $0.1 - 0.27$, we calculate the isotropic gap Δ vs T curves at 3 GPa. As shown in Fig. S2, the estimated T_c value decreases almost linearly with increasing μ^*. Therefore, the estimated value of $T_c = 11.5$ K with $\mu^* = 0.27$ comes close to the experimental data [6,7] of $\approx$8 K at the QCP of $\approx$2 GPa. However, the ratio $2\Delta_{T=0}/k_B T_c$ hardly changes with respect to μ^* [see Fig. S2(b)]. We note that, although the experimental values of T_c are well reproduced by the present harmonic approximation with $\mu^* = 0.27$, the proper μ^* value would be lowered by including anharmonic phonons [63].

[63] I. Errea, F. Belli, L. Monacelli, A. Sanna, T. Koretsune, T. Tadano, R. Bianco, M. Calandra, R. Arita, F. Mauri, and J. A. Flores-Livas, Quantum crystal structure in the 250-kelvin superconducting lanthanum hydride, Nature (London) **578**, 66 (2020).

[64] We note that the present superconducting gap function predicted by the anisotropic Migdal-Eliashberg formalism without vertex corrections [65] has sufficiently larger values of Δ_i, compared to $2\alpha_i\Delta_i$. Therefore, we believe that vertex corrections would be unlikely to produce a nodal gap in CsV_3Sb_5.

[65] F. Schrodi, P. M. Oppeneer, and A. Aperis, Unconventional superconductivity mediated solely by isotropic electron-phonon interaction, Phys. Rev. B **104**, L140506 (2021).

[66] According to the tight-binding calculation of the two-dimensional ideal kagome lattice, the saddle points located at the M point produce their corresponding van Hove singularities (VHSs) with the logarithmically diverging density of states [see Fig. S5(a)], thereby leading to the Fermi surface nesting of VHSs at the van Hove filling. However, for the pristine phase of CsV_3Sb_5 under pressure, the saddle points at the M point do not give rise to VHSs in the total DOS [see Fig. S5(b)]. Note that the two saddle points SP_1 and SP_2 below E_F change their energy positions very little as a function of pressure (see Fig. S6). Therefore, the saddle points near E_F are unlikely to play an important role in the pressure-induced change of T_c. Instead, as shown in Fig. 3(c), the softening of the L_i and M_i phonon modes with decreasing pressure significantly influences the EPC constant, forming a superconducting dome around the QCP. Moreover, the low-frequency limit of the imaginary part of electronic susceptibility, defined as $\mathrm{Im}[\chi_0(q)] = \sum_{nm}\int d\mathbf{k}\delta(\varepsilon_{n\mathbf{k}} - E_F)\delta(\varepsilon_{m\mathbf{k}+\mathbf{q}} - E_F)$, does not exhibit a dominant peak at the M point (see Fig. S7), indicating no indication of the Fermi surface instability due to saddle points. Based on these results, we conclude that electron correlation effects due to the Fermi-surface nesting of VHSs between three distinct M points are unlikely to induce unconventional superconductivity in CsV_3Sb_5 around the QCP.

[67] Since the electronic structures and phonon spectra of RbV_3Sb_5 and KV_3Sb_5 are similar to those of $CsV3Sb_5$ [59], their superconducting states can also be explained by a conventional phonon-mediated s-wave pairing mechanism.